



ORIGINAL RESEARCH ARTICLE

Electrochemical Properties of CrAl/CrAlN and CrAl/CrAlN-(a-CN_x) Multilayer Deposited by High Power Impulse Magnetron Sputtering

C.J. Martínez-González, M. Flores-Jimenez, J. Pérez-Alvarez, O. Jimenez, and M. Flores

Submitted: 28 January 2023 / Revised: 16 June 2023 / Accepted: 5 July 2023 / Published online: 24 July 2023

The corrosion resistance of two multilayered metallic/ceramic coatings deposited from a 50:50 vol.% CrAl target, with a-CN_x top layer deposited by High Power Impulse Magnetron Sputtering (HIPIMS) onto A11 tool steel was studied. The CrAl/CrAlN multilayer coatings with, and without a-CN_x top layer, characterized by FE-SEM resulted in two different layers thicknesses of 1.5 and 1.2 μm, respectively. A glassy-like morphology was observed in the CrAl layer and in the CN_x top layer, whereas the CrAlN layers exhibited a columnar morphology. XRD-analysis revealed a CrAlN FCC structure (111), accompanied of a Cr phase (110). Raman spectra for the CN_x top layer, showed the characteristic peaks of G (Graphitic) and D (Disorder) for molecular vibrations in a-CN_x containing thin films. Peaks were located between 1200 and 1700 cm⁻¹. XPS results, on the other hand, showed the characteristic peaks for Cr, Al, N, present in both coatings. The deconvoluted peaks agreed with Cr2p3/2, Al2p, and N1s binding energies, respectively; besides; XRF analysis confirms the bulk chemical composition of these coatings. The electrochemical impedance, and potentiodynamic polarization tests in a 3.5 wt.% NaCl solution, displayed an improvement in the corrosion resistance for a-CN_x top layer, and up to 15 times in R_p values compared to AISI A11 substrate.

Keywords carbon nitride, chromium aluminum nitride, corrosion, HIPIMS PVD thin films

1. Introduction

In many industrial applications like milling, turning steel and high-speed cutting, there is a need of protecting industrial tools with nitride hard coatings to overcome the problems associated with high temperatures, oxidation and corrosive environments, and extend the service life of these tools (Ref 1-3). PVD techniques are widely used to deposit thin films with good adherence to the substrate at low temperatures to avoid microstructural damage in the substrate (Ref 4). Transition metal nitride coatings like TiN (Ref 5, 6) and CrN (Ref 7, 8), as well as amorphous carbon (a-C) are widely used to provide anti-corrosion protection (Ref 9-11). Compared to TiN, CrN-

based thin films provide superior wear and corrosion resistance with high toughness (Ref 7). CrN thin films have been successfully applied to coating industrial components from molding dies, cutting tools, including metal processing devices (Ref 12). However, it is well known that CrN/metal deposited by sputtering present a columnar morphology which is a disadvantage for some mechanical properties where grain boundaries, micropores, valleys and cracks forming during PVD deposition process, can serve as paths for corrosive ions in solution through the substrate (Ref 9, 13). It has been reported that CrN-based films plus another metals such as Al, Si, B, and Ti, suppress the columnar growth of CrN coatings (Ref 14). The deposition of CrAlN thin films form a ternary system, that improves mechanical, tribological, corrosion resistance and thermal stability (Ref 7, 14-18). However, some studies found a critical thickness when CrAlN films are deposited through co-sputtering from a binary target composed of chromium (99.95%) and aluminum (99.99%), due to decreased corrosion resistance when the layer thickness reached up to 2.7 μm, and emergence of phases prone to corrosion (Ref 15). Besides, other studies of CrAlN layers obtained with one Cr/Al target (50/50 at.%) or with two targets (Cr and Al) deposited by magnetron sputtering, the film deposited from one homogeneous target showed low frictional coefficient and a columnar morphology; however, those deposited from two targets have better control over the chemical composition, dense morphology, higher hardness and improved Young's modulus (Ref 19). Some researchers suggest a multilayer architecture, to enhance the mechanical and tribological properties, fracture toughness and the mechanical behavior, as well as the corrosion resistance of the films (Ref 20). Compared with single layer films, multilayers have more interfaces, that

C.J. Martínez-González, Centro Universitario de Ciencias Exactas e Ingenierías, Universidad de Guadalajara, Blvd. Marcelino García Barragán 1421, Olímpica, 44430 Guadalajara, Jalisco, Mexico; and Maestría en Ciencia e Ingeniería de los Materiales, Quantum-Ciudad del Conocimiento, Universidad Autónoma de Zacatecas, Av. Marie Curie, 1000 Blv. El Bote, Col. Ciudad Argentum, 98047 Zacatecas, Zac., Mexico; **M. Flores-Jimenez**, Ingeniería Mecánica Agrícola, Universidad Autónoma de Chapingo, Carretera Federal México- Texcoco Km 38.5, 56230 Texcoco, Edo. de México, Mexico; and **J. Pérez-Alvarez, O. Jimenez, and M. Flores**, Departamento de Ingeniería de Proyectos, CUCEI, Universidad de Guadalajara, Jose Guadalupe Zuno 48, Los Belenes, 45150 Zapopan, Jalisco, Mexico. Contact e-mail: omar.aleman@academicos.udg.mx.

decrease the number of defects, enhancing the crack and corrosion resistance (Ref 21). A multilayer of CrAl/CrAlN coating deposited by magnetron co-sputtering pulsed DC method with a target Cr/Al (25/75 at.%) area ratio, showed compressive stress when bilayer period was reduced. XPS analysis showed that the elemental concentration of CrAlN films is controlled by the applied power in the target and Ar/N₂ gas ratio (Ref 22). On the other hand, CrAlN multilayer films were doped with elements such as Si to modify its microstructure, restricting the grain growth, or adding an amorphous CN_x structure to increase the corrosion resistance in NaCl solution (Ref 9, 10, 20). More recently, researchers have investigated the structure and properties of CrN-based films deposited through high power impulse magnetron sputtering (HIPIMS), such coatings showed a dense defect-free structure morphology (Ref 23-25). HIPIMS is known to allow high ion densities in the plasma, with a relatively small deposition rate. On the contrary, HIPIMS coatings have shown higher density in comparison to other PVD techniques (Ref 26, 27). Also, coatings with a refined structure and lower residual stresses and higher hardness can be obtained (Ref 13, 26). Some results have been used for industrial applications for the improvement of coatings used in the plastic processing industry (Ref 28). Besides, some studies were directed to improve the corrosion resistance of multilayer coatings by adding a CN_x top layer, deposited through HIPIMS technique (Ref 9, 10). However, investigations regarding the corrosion resistance of metallic/ceramic multilayer coating by HIPIMS are still limited. The aim of this research is to improve the corrosion resistance of an AISI A11 tool steel by means of a two architecture CrAl/CrAlN multilayer coating from sectioned targets (Cr:50-Al:50), and the effect of an amorphous a-(CN_x) top layer deposited by HIPIMS.

2. Material and Methods

2.1 Deposition by HiPIMS

AISI-A11 tool steel substrates were tempered (55 HRC), and polished until reaching a roughness of Ra = 40 nm. Silicon wafers were also used as substrates (99.999% purity, crystal orientation $\langle 111 \rangle \pm 0.5^\circ$). Both substrates were cleaned in an ultrasonic bath in acetone and absolute alcohol, 15 min. each. Subsequently, samples were dried with a flux of N₂ to prevent oxidation. CrAl/CrAlN multilayer coatings were grown from a 50:50 vol.% CrAl target (2-inch diameter and 99.95% purity) while C target (2 inch in diameter and 99.95% purity) was used for the a-CN_x top layer in the presence of argon and nitrogen (99.999%), serving as working and reactive gas, respectively. All substrates were fixed at 70 mm from each magnetron, substrates were grounded at the substrate holder. Before deposition, the chamber was evacuated to a base pressure of 3.99×10^{-4} Pa. The targets were cleaned through DC current during 2 h, at a working pressure of 0.66 Pa with an Ar flow rate of 20 sccm. Followed by a HIPIMS clean up using deposition parameters (see Table 1) before the multilayer deposition process. Architecture and all the HIPIMS parameters are summarized in Table 1. CrAl layer was grown at 0.66 Pa with an Ar flow rate of 20 sccm. CrAlN layer was deposited in a reactive N₂ flow rate of 13.5 sccm in a 1.48 Ar/N₂ ratio, same parameters were used for the a-CN_x top layer. Deposition temperature was around 110 °C ± 5 , and no substrate bias

voltage was used. First, multilayer architecture was formed alternating eight CrAl/CrAlN layers and labeled as *S4* (see Table 1b), meanwhile, multilayer *S5* was composed by six alternated CrAl/CrAlN layers and a top CN_x layer.

2.2 Structure, Morphology and Chemical Characterization

Phase characterization of coatings was assigned using x-ray diffraction by means of a D8 Advance Bruker diffractometer with a Cu-K α Cu radiation ($\lambda = 1.5418$) with an energy of 30 kV, 30 mA and 0.01°/s as the scan rate in a 2θ range of 30-90°. The morphology and thickness were evaluated from cross-sectional images by using a Field Emission Scanning Electron Microscope (Tescan MIRA 3 LMU). The a-CN_x top layer was analyzed by Raman spectroscopy using a confocal microscope (DXR, Thermo Scientific) with a 532 nm laser wavelength. A chemical bond was analyzed for each CrAl and CrAlN layer deposited separately in silicon substrates, by means of X-ray photoelectron spectroscopy (XPS) with a monochromatic source Al K-alpha beam energy 1486.7 eV, power of 250 W and 12.5 kV. The x-ray fluorescence (XRF) analysis of multilayers were performed by a S2 PUMA Series 2 spectrometer.

2.3 Electrochemical Test

The electrochemical properties were evaluated by potentiodynamic polarization (PP) and electrochemical impedance spectroscopy (EIS), using a potentiostat/galvanostat (Corrtest CS350). A three-electrode cell was used in NaCl 3.5 wt.% at room temperature (25 °C). The Open Circuit Potential (OCP) was recorded for 60 min. The PP tests were carried out at a scan rate of 0.16 mV/s from -1 to 1 V versus OCP; while the EIS tests were recorded on wide range of frequencies from 1 MHz to 0.1 Hz with 20 mV of amplitude at same configuration used in PP tests.

3. Results and Discussion

3.1 Structure and Morphology

The diffractograms of *S4* and *S5* samples are seen in Fig. 1(a), and (b). In both samples, (111), (200), (220) and (222) diffraction peaks are observed, corresponding to CrN NaCl type crystal structure (Ref 12, 14). In both samples, AlN phase (200), (220), and (111) were observed, but with less intensity. However, CrAlN phase is commonly associated with CrN diffraction peaks, hence CrAlN films have a predominant cubic structure, these results are in agreement with those reported previously (Ref 22, 29, 30). Samples *S4* and *S5*, exhibited an FCC structure of CrAlN (JCPDS 25-1495); however, sample *S5* exhibited peaks with different intensity, which could be attributed to the a-CN_x top layer. These results agree well with those reported previously (Ref 9, 15, 19, 31).

Additionally, Fig. 1(c) shows the Raman spectra for the CN_x top layer, where characteristics peaks of D (Disorder) and G (Graphitic) for molecular vibrations in a-CN_x thin films are located between 1200 and 1700 cm⁻¹. The peak centered at 1375 cm⁻¹ is associated to disordered band (D), meanwhile, graphitic band (G) is located at 1562 cm⁻¹. Similar Raman results have been observed for pure carbon films, which are associated to *sp*² C sites (Ref 32, 33). Studies in amorphous

Table 1. a) Multilayer HIPIMS parameter and b) multilayer architecture

Sample ID	Layer		Pulse width, μs	Frequency, Hz	Voltage, V	Peak current, A	Peak power density, W/cm^2	Thickness/period, nm	Time, min
	Periods	Composition							
a)									
<i>S4</i>	4	CrAl	20	300	610	34	1,023	155	12
	4	CrAlN	20	300	420	50	1,036	235	45
<i>S5</i>	1 top layer	CN _x	30	300	735	53	1,921	85	13
	3	CrAl	20	300	610	34	1,023	155	12
	3	CrAlN	20	300	420	50	1,036	235	45

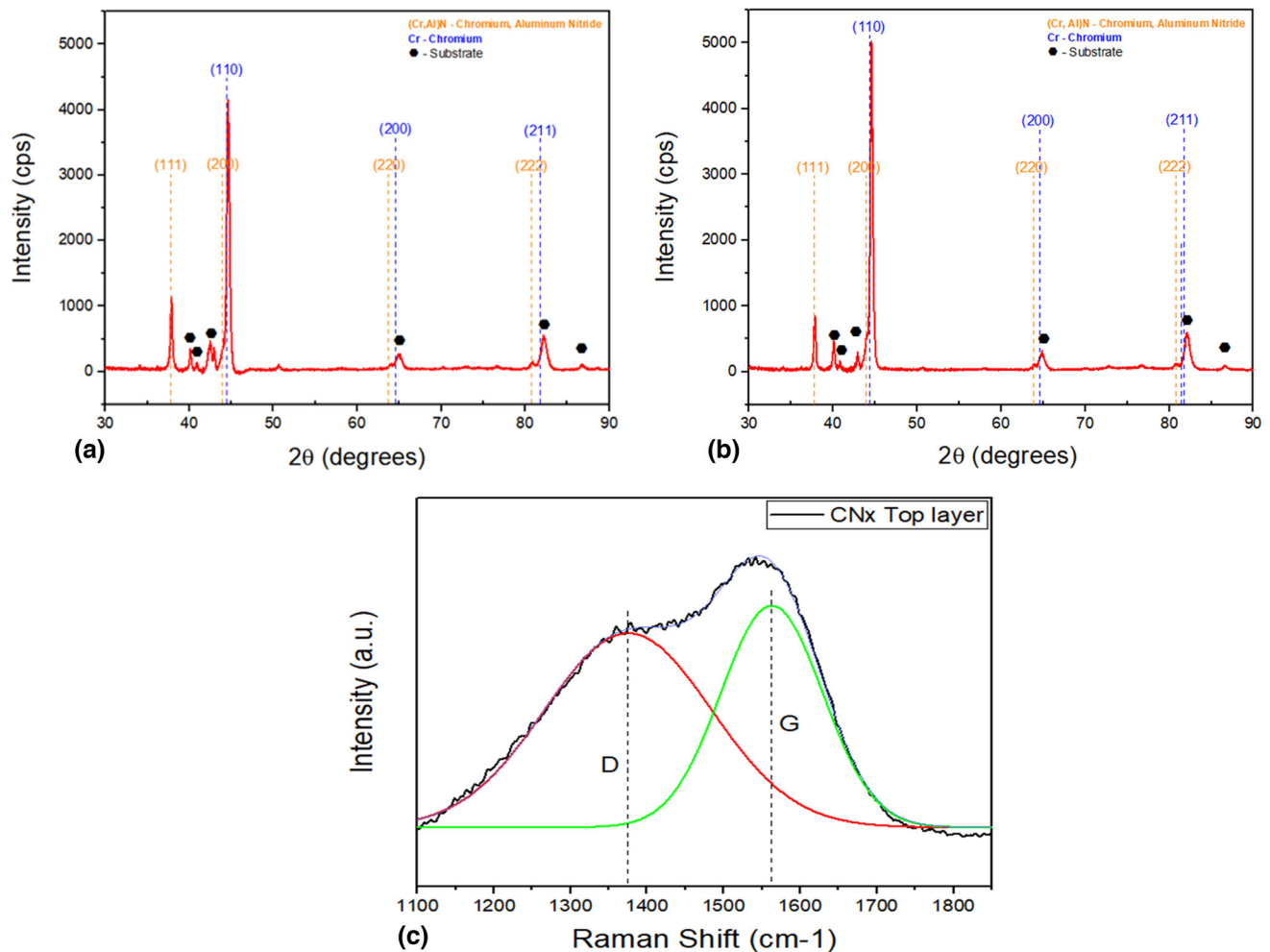
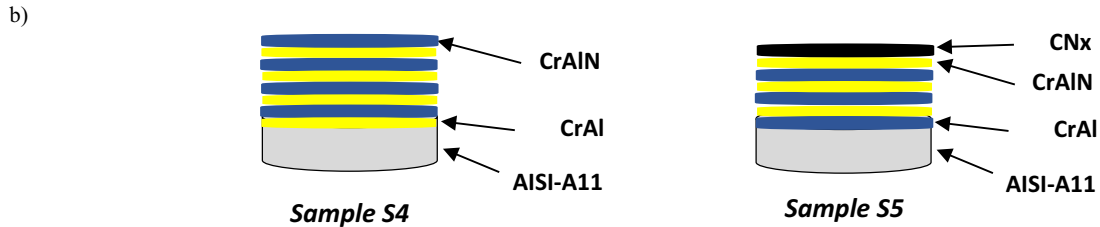


Fig. 1 XRD diffractograms: (a) for sample *S4* and (b) for sample *S5*. Raman spectrum: (c) CN_x top layer

carbon nitride coatings showed that the G band appear by the C–C stretching vibrations of sp^2 bonds, meanwhile D band is associated to breathing modes in both sp^2 rings and chains (Ref

34). Those peaks were fitted with a Gaussian deconvolution. A glassy morphology was observed for the CrAl layer (*S4* sample, Fig. 2a) and in the a-CN_x top layer (*S5* sample, Fig. 2b), as has

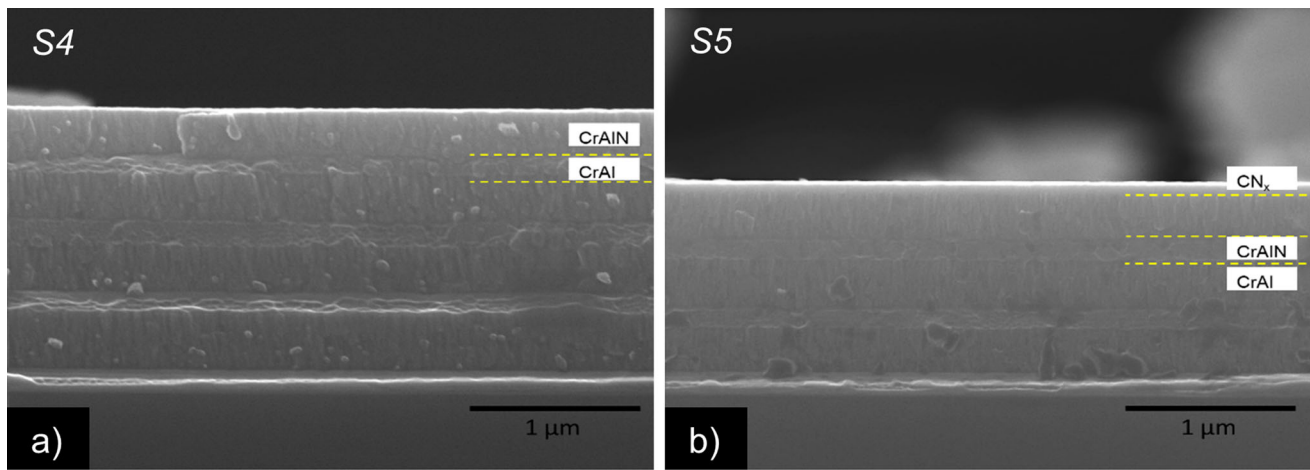


Fig. 2 SEM cross section micrographs: (a) Sample *S4* and (b) Sample *S5*

been reported in other studies (Ref 10, 22, 35). However, CrAlN layers presented the characteristic columnar morphology (Ref 13, 28). Both samples presented a total thickness of 1.5 and 1.2 μm , respectively.

3.2 Chemical Characterization

Figure 3 and 4 shows XPS spectra of *S4* and *S5* coatings. The binding energies of all elements were calibrated by referencing the *Cl*s peak at 284.8 eV. And XPS spectra were fitted using Gauss-Lorentzian peak shapes, all the samples were ion eroded before XPS measurements. Figure 3(a) shows the XPS survey spectrum for CrAl/CrAlN films, the peaks at 575.8, 533, 397.8, 285.2, 118.2, 74.0, and 42.7 eV corresponded to *Cr2p3/2*, *O1s*, *N1s*, *Al2s*, *Al2p*, and *Cr3p* binding energies, respectively. As shown in Fig. 3(b), the high-resolution spectrum of *Cr2p* is composed of spin doublets, separated by 9.3 eV. The XPS spectrum *Cr2p3/2* was deconvoluted in four peaks, located at 575.2 eV representing a CrAlN phase, peak at 576.9 eV for CrN phase and for 579.9 eV *Cr2O3* phase, respectively, meanwhile 585.4 eV corresponding to *Cr2p1/2*. Some researchers reported two peaks for the *Cr2p* (575.6 and 578.3 eV) associated with Cr–N and Cr–O3 bonds and the second one (585.5 eV) assigned to Cr–N bond (Ref 22, 35). Figure 3(c) showed *Al2p* spectrum, deconvoluted in three peaks with the characteristic peaks, at binding energy 73.4 eV for CrAlN phase, another peak at 74.0 eV from AlN phase and the peak 78.5 eV represents *Al2O3* phase (Ref 22, 35–37). Finally, as is seen in Figure 3(d), the deconvoluted spectrum of *N1s* showed a peak at 396.5 eV related to CrN phase, followed by a weaker peak at 399 eV from *N1s* (Ref 38, 39).

Figure 4(a) shows the XPS survey spectra for CN_x top layer in sample *S5*, peaks at 531.7 eV, 398.5 eV, and 285.2 eV from *O1s*, *N1s*, and *Cl*s binding energies, respectively. As can be seen in Figure 4(b), high-resolution spectrum for *Cl*s is deconvoluted in three peaks centered at 285.0 eV for *sp2C–N*, 286.1 eV from *sp3C–N* and 288.2 eV representing C–O. The *N1s* spectrum in Figure 4(c) was deconvoluted into two peaks centered at 398.9 eV for *N–sp3 C* bonds and 400.2 eV from *N–sp2 C* bonds (Ref 40, 41). The core electronic spectra carry information of the chemical composition of the CrAl/CrAlN films, the concentration measurements and identification of specific bonding were the result of the integral of *O1s*, *N1s*, *Cl*s, *Al2p3/2*, and *Cr2p3/2* spectra, to measure concentrations

of Cr, Al, N, and C elements. The deconvoluted peaks were used to estimate the bond contents, according to the following equation (Ref 42):

$$C_i = \frac{\sum(A_i/S_i)}{\sum(A_j/S_j)} \quad (\text{Eq 1})$$

Where *S* is the sensitivity factor, *A* is the integral of deconvoluted peaks, and *C* is the atomic content. Numerator part is the sum of the integral of one sort of bond, denominator part is the sum of the integral of all types of bonds decomposed from the whole peak of *O1s*, *N1s*, *Cl*s, *Al2p3/2*, and *Cr2p3/2* spectra. Atomic concentration of CrAl, CrAlN, and CN_x films are listed in Table 2. The XPS results reveal that Cr and Al atoms have bonded with N atoms to form nitrides, the atomic concentration (see Table 2) obtained by XPS for sample *S4* and *S5*, is under the theoretical maximum solubility of fcc-AlN in the fcc-CrN which is around 77% (Ref 43, 44). XRF results of the bulk chemical composition is listed in Table 3 and agreed well with the XPS superficial atomic concentration obtained in sample *S4*; however, sample *S5* shows a light discrepancy for the Cr and Al concentration, which is attributed to the equipment limitation to quantify light elements. And the sputtering yield of Cr and Al species when reactive atmosphere is deposited (Ref 22, 45, 46). Similar results have been observed from EDS-SEM analysis (Ref 30, 46, 47).

3.3 Corrosion and Electrochemical Resistance

The PP curves for the AISI-A11 substrate and multilayer coatings are presented in Figure 5(a). For the AISI-A11 in 3.5 wt.% NaCl a shift on the anodic curve was observed when the potential reaches the range between -0.631 and -0.511 V, owing to the passivation layer formation until its dissolution followed by a formation of a second passivation layer with an increment in the current density, similar results were mentioned in some studies (Ref 15, 48). The anodic shift in the sample *S4* could be due to the formation of a weak passivation film in the potential range of -0.599 and -0.538 V. This behavior has been observed before, and is associated to CrAlN coatings surface defects (Ref 20). It is seen that multilayer coatings enhanced the corrosion resistance of the AISI-A11 substrate. Computed values are presented in Table 4, where *E_{corr}* more positive values are related to anti-corrosion properties hence, sample *S5* has the highest *E_{corr}* values (-0.478 V). Besides,

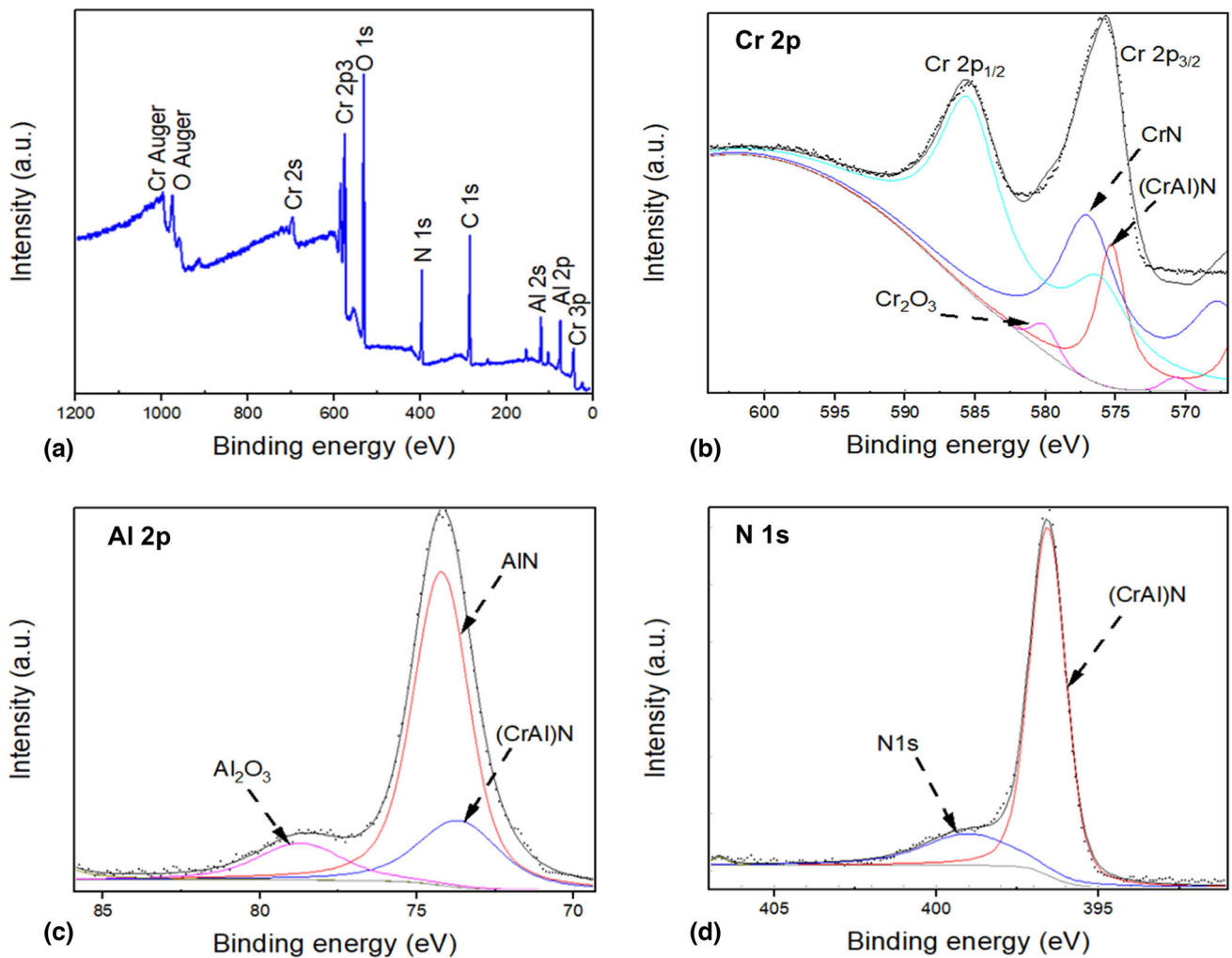


Fig. 3 XPS survey spectra: (a) CrAl/CrAlN films, and high resolution for (b) Cr, (c) Al, and (d) N

lower corrosion density values of $1.301 \text{ } (\mu\text{A}/\text{cm}^2)$, compared to 2.586 and $19.46 \text{ } (\mu\text{A}/\text{cm}^2)$ for sample *S4* and AISI-A11, respectively. Where higher I_{corr} value means higher corrosion rate once corrosion started. Polarization resistance of the different alloys is inversely proportional to corrosion current density and directly proportional to their corrosion potentials, hence, sample *S5* shows higher polarization resistance (R_p) of $4.070 \text{ k}\Omega \text{ cm}^2$ compared to sample *S4*, these results are attributed to the addition of a- CN_x top layer (Ref 10).

Nyquist plots exhibit single semicircles in all tests, without degradation of the samples in NaCl solution. Figure 5(b), shows the semicircles for AISI-A11 steel and coated samples *S4* and *S5*, as can be seen for sample *S5*, the semicircle is larger in comparison to *S4*. Therefore, a ceramic behavior of the multilayers with the a- CN_x top layer, indicates an improvement in the corrosion resistance, followed by the sample *S4* (CrAl/CrAlN) multilayer without the a- CN_x top layer, both samples coated improved the corrosion resistance of AISI-A11 steel.

The Bode plots revealed the phase angle as a function of the frequency that is used to confirm Nyquist data. EIS results postulate two different interfacial reactions related to coating-solution interface and substrate-coating interface. Figure 5(c) sample *S5* displays the broadest frequency range (0.04-2000 Hz) with a decrease of the phase angle to -49° , this increment is related to a stable passive layer due to the CN_x top

layer. Sample *S4* shows a medium range of frequency (0.02-1000 Hz) with a phase angle of -36° corresponding to a weak passive layer that seems to be dissolved near to a phase angle of -18° and starts to form again. Compared to AISI-A11 steel with two range frequencies (1-1000 Hz and 0.01-1 Hz) with a phase angle of -15° and -7° , respectively. Which is due to the formation and dissolution of a passive layer over the substrate. The above results, confirms that sample *S5* with a CN_x top layer provides more protection as an ideal capacitor at a broader frequency range to prevent the substrate from corrosion, compared to sample *S4*. Where the corrosion behavior of CrAl/CrAlN multilayer could be deteriorated due to AlN formation (Ref 14).

On the other hand, a high modulus of impedance (Z) of $450 \text{ }\Omega\text{cm}^2$, was obtained for sample *S5* with a low frequency (0.01-20 Hz), as is seen in Fig. 5(d), followed by sample *S4* with a module of impedance of $125 \text{ }\Omega\text{cm}^2$ for a low range frequency (0.01-10 Hz). Finally in Fig. 5(e) shows the open circuit potential values for sample *S4* and *S5*. It is clear the influence of the CN_x top layer on the OCP values, where these values implies that the corrosion probability on sample *S5* is lower than sample *S4*. Thus, the CN_x top layer provided an excellent protection to the substrate AISI-A11 in corrosion environments.

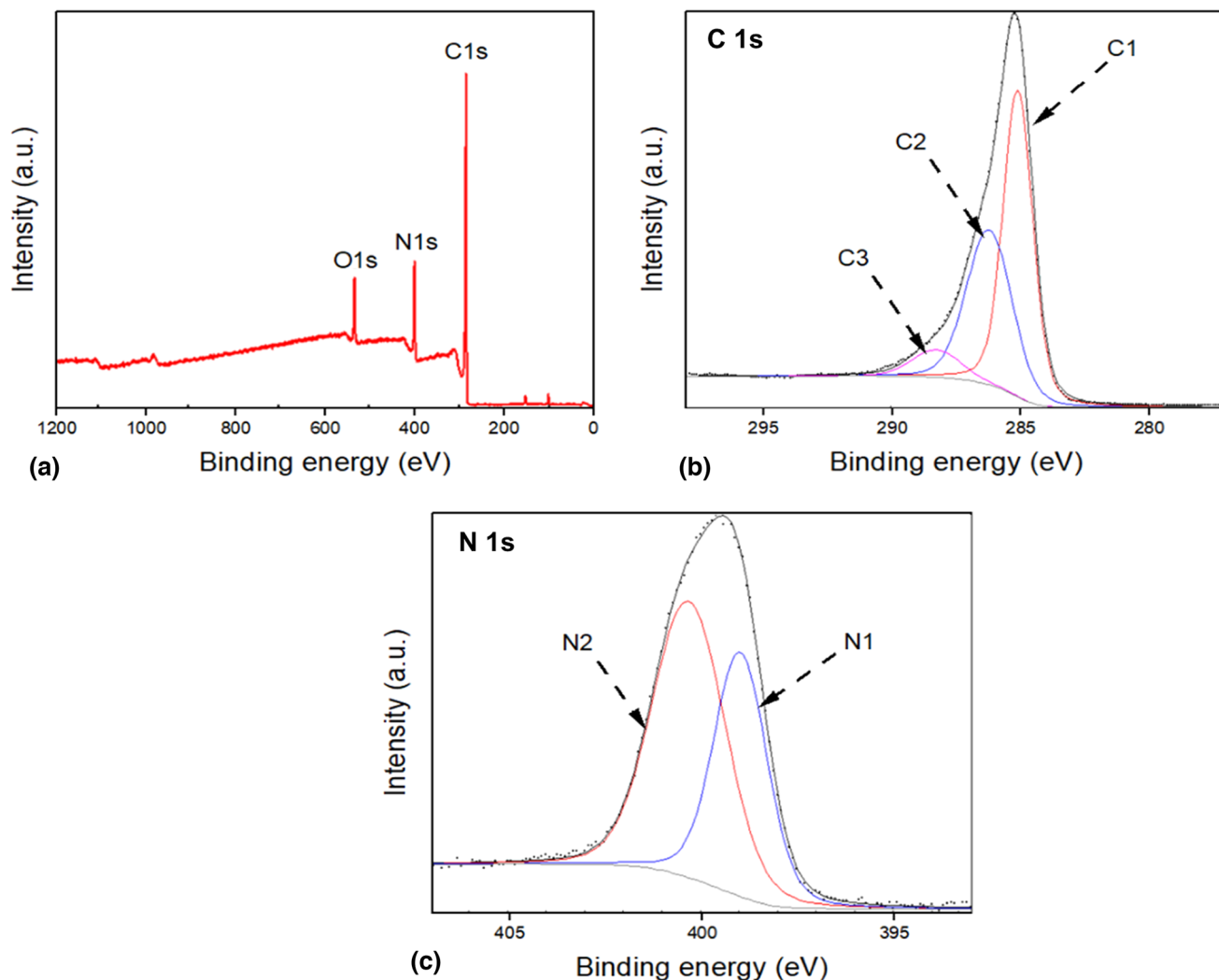


Fig. 4 XPS survey spectra: (a) CN_x film, and high resolution for (b) C, and (c) N

Table 2 Atomic composition by XPS of films in sample *S4* and *S5*

Atomic composition, at.%			
Cr	Al	N	(Cr + Al)/N
33.53	66.46
56.38	26.26	17.35	4.76
C			N
84.72			15.27

The equivalent circuits proposed for the substrate and multilayers is presented in Fig. 6. Fitting values results for substrate and two coated samples are listed in Table 5. The R_s is the electrolyte solution between the working and reference electrodes, R_{po} corresponds to the pore resistance, related to the block effect of the coating to inhibit the electrolyte penetration. As is seen in Table 5, sample *S5* had the highest R_{po} value ($14 \Omega cm^2$), while sample *S4* shows a R_{po} value of ($6.15 \Omega cm^2$). In Table 5, the n values are related to the surface

Table 3 XRF atomic bulk composition of multilayers of sample *S4* and *S5*

Sample ID	Atomic composition, at.%		
	Cr	Al	N
<i>S4</i>	32.46	66.30	...
<i>S5</i>	27.52	69.74	...

coating quality, where sample *S4* presents the highest value (0.726) and the low n values corresponding to sample *S5* (0.657); however, the columnar morphology in sample *S4* (CrAl/CrAlN) is characterized to allow the pass of the electrolyte through the substrate (Ref 49-51). Compared to the non-smooth CN_x top layer in sample *S5*, that affected the corrosion behavior. On the other hand, R_{ct} values are related to charge transfer resistance due to the formation of a double layer of charge at the substrate-electrolyte interface, then a high R_{ct} value indicates the lower transfer rate of the electron. Sample *S5* shows the highest value ($502.5 \Omega cm^2$), followed by a minor value for sample *S4* ($98.08 \Omega cm^2$). Finally, the polarization

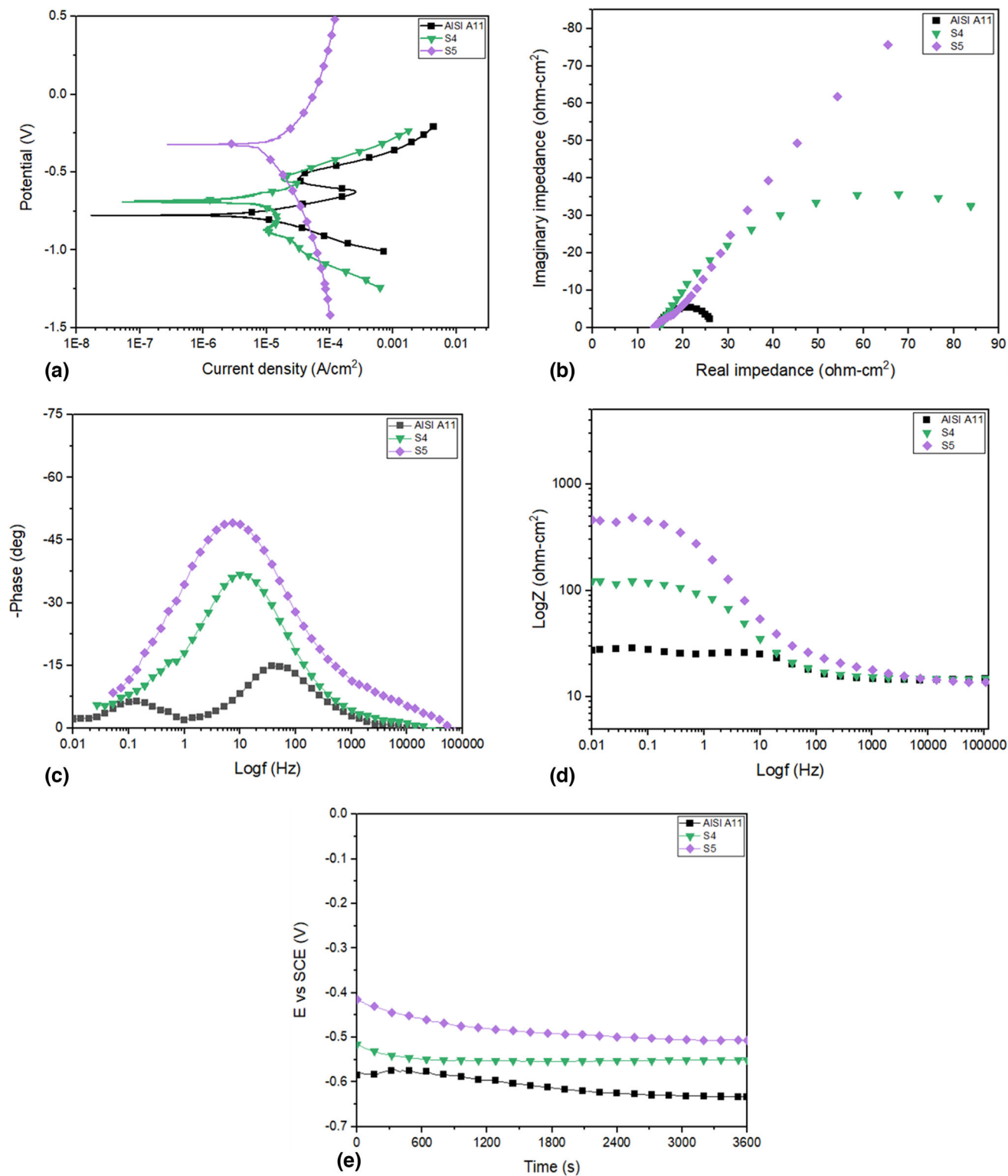


Figure 5 Electrochemical analysis plots: (a) The Tafel curves, (b) Nyquist curves, (c) Bode curves evaluation of phase as function of logf (Hz) and (d) Bode plot of LogZ as function of Logf (Hz) and (e) Open circuit potentials evolution of samples as a function of exposure time for AISI A11 steel substrate and multilayer sample *S4* and *S5* in NaCl solution.

resistance (R_p) which is the sum of all resistance in the EIS results shows higher value for sample *S5* ($530.35 \Omega\text{cm}^2$) compared to sample *S4* ($118.86 \Omega\text{cm}^2$). Porosity ratio obtained from the measured polarization resistance R_p at given potential (Ref 52).

$$P = \frac{R_{ps}}{R_{pc}} \quad (\text{Eq 2})$$

where R_{ps} is the polarization resistance of the substrate and R_{pc} corresponds to the coating. According to Eq 2, sample *S5*

(0.0520) has a low porosity ratio value, compared to sample *S4* (0.2324) as is seen in Table 5. Then, these R_{po} and R_{ct} and R_p values for sample *S5*, which is related to a coating with more compactness than sample *S4* and better corrosion properties (Ref 53). Figure 7 shows the surface morphology after the electrochemical tests. Figure 7(a), (b), and (c), shows the corrosion zone for sample *S4* and some magnified zones, where small pitting holes were observed. On the other hand, Fig. 7(d), (e), and (f) corresponding to sample *S5*, a delamination is clearly observed over the coating after electrochemical tests. Similar results were reported for CrAlN based, single and multilayered coatings (Ref 14, 20, 50).

Figure 8 shows the Raman spectra analysis performed in the corrosion track surface for both samples. The analysis was carried out into the corrosion zone (CZ) and corrosion line (CL), surrounded by dotted line, respectively. Figure 8a) shows the Raman analysis in the CZ for sample *S4*, where bands at 698 and 1547 cm^{-1} were seen. The Raman analysis for the CL, presented only a weak peak at 735 cm^{-1} . According to other studies, peak at 698 cm^{-1} corresponds to chromite (FeCr_2O_4) (Ref 54). The Raman spectra pattern for chromite consist of a major peak located around 685 cm^{-1} accompanied of a shoulder weak peak near to 650 cm^{-1} , and a second peak near to 555 cm^{-1} . Chromite belongs to the spinel group of minerals (Ref 55), where typically chromium substitutes for aluminum or iron (3+) in the crystal lattice. On the other hand, a width peak around 650 cm^{-1} also is attributed to CrAlN Raman spectra as previously reported (Ref 22). At high wavelengths of 1547 cm^{-1} a peak is also observed. Similar results were observed during graphitic corrosion, when the metallic constituents of gray iron or steel are selectively removed or converted into corrosion products (Ref 56).

Figure 8c corresponding to the Raman analysis in the CZ obtained in sample *S5*, shows a weak peak at 723 cm^{-1} ,

followed of two intense peaks at 1379 and 1563 cm^{-1} and finally a peak at 2833 cm^{-1} . The peak at 723 cm^{-1} is attributed to chromite, where a change in the peak locations, is related to a change in the chromium and aluminum (iron) (Ref 54). The peaks between 1350 and 1550 cm^{-1} , are the characteristic peaks of thin films of a-CN_x (Ref 33, 57, 58). And the peak at 2833 cm^{-1} , corresponds to the Al₂O₃ Raman spectra (Ref 59), these results agree well with the XPS analysis obtained previously (see Fig. 3c). The last Fig. 8(d), shows the peaks for CL where the same peaks around 725, 1376, 1545, and 2814 cm^{-1} were observed. Raman analysis can be related to elemental concentration as other studies have shown (Ref 54). Varies chromite samples were analyzed, and the chromium number (#Cr), which was calculated as $\text{Cr} = \text{Cr}/(\text{Cr} + \text{Al})$. Where the results, the main peak for the chromite is located at the range of 707 to 727 cm^{-1} , and is related to a chromium number of 0.555. Those results agree well with the atomic concentration obtained from the XPS analysis (see Table 2), when CrAlN layer is deposited in both samples.

4. Conclusions

The CN_x top layer showed a glassy morphology over CrAl/CrAlN layers with columnar morphology, with a preferential orientation (111), (200), (220), and (222).

XPS measurements are in agreement with XRD phases detected and the clear incorporation of Al into the CrN. XPS survey spectra for CN_x top layer, confirm the presence of sp²C-N, sp³C-N, and C-O bonds for carbon. And N-sp³ C and N-sp² C bonds for nitrogen. CN_x bonds are in agreement with Raman measurements and characteristics peaks of G and D and the relation I(D)/I(G) attributed to the formation of carbon sp² bonds.

The electrochemical behavior in NaCl solution observed in PP and EIS analysis, reveals an increment in the corrosion resistance for HIPIMS coatings and the better performance was acquired with a-CN_x top layer. The coatings showed an improvement in (R_p) values for sample *S5*, up to 15 times compared to uncoated substrate. Additionally, the Bode and Nyquist plots, confirmed that *S5* with a CN_x top layer provides more protection compared to sample *S4*.

The equivalent circuit proposed indicates that sample *S5* has a greater density than sample *S4* and better corrosion properties

Table 4. Tafel fitting values obtained from the potentiodynamic polarization test

Sample ID	E_{corr} , V	I_{corr} , $\mu\text{A}/\text{cm}^2$	B_a , V	B_c , V	R_p , $\text{k}\Omega \text{cm}^2$
AISI-A11	-0.714	19.46	0.020	0.030	0.271
<i>S4</i>	-0.684	2.586	0.027	0.022	2.035
<i>S5</i>	-0.478	1.301	0.023	0.024	4.070

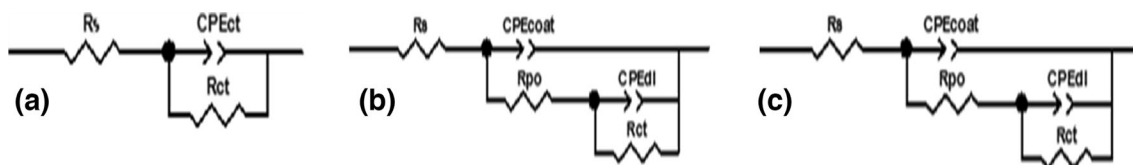


Figure 6 Schematic of the equivalent circuit model use to fit impedance EIS data: (a) AISI-A11 steel, (b) Sample *S4* and (c) Sample *S5*

Table 5 Equivalent circuit values obtained from electrochemical impedance spectroscopy analysis

Sample ID	R_s , Ωcm^2	CPE_{coat} , Fcm^{-2}	n	R_{po} , Ωcm^2	CPE_{dl} , Fcm^{-2}	n	R_{ct} , Ωcm^2	R_p , Ωcm^2	P
AISI-A11	14.47	89.77×10^{-5}	0.830	13.16	27.63	...
<i>S4</i>	14.63	1.02×10^{-3}	0.726	6.15	1.16×10^{-4}	0.919	98.08	118.86	0.2324
<i>S5</i>	13.85	4.05×10^{-4}	0.657	14	2.48×10^{-4}	0.807	502.5	530.35	0.0520

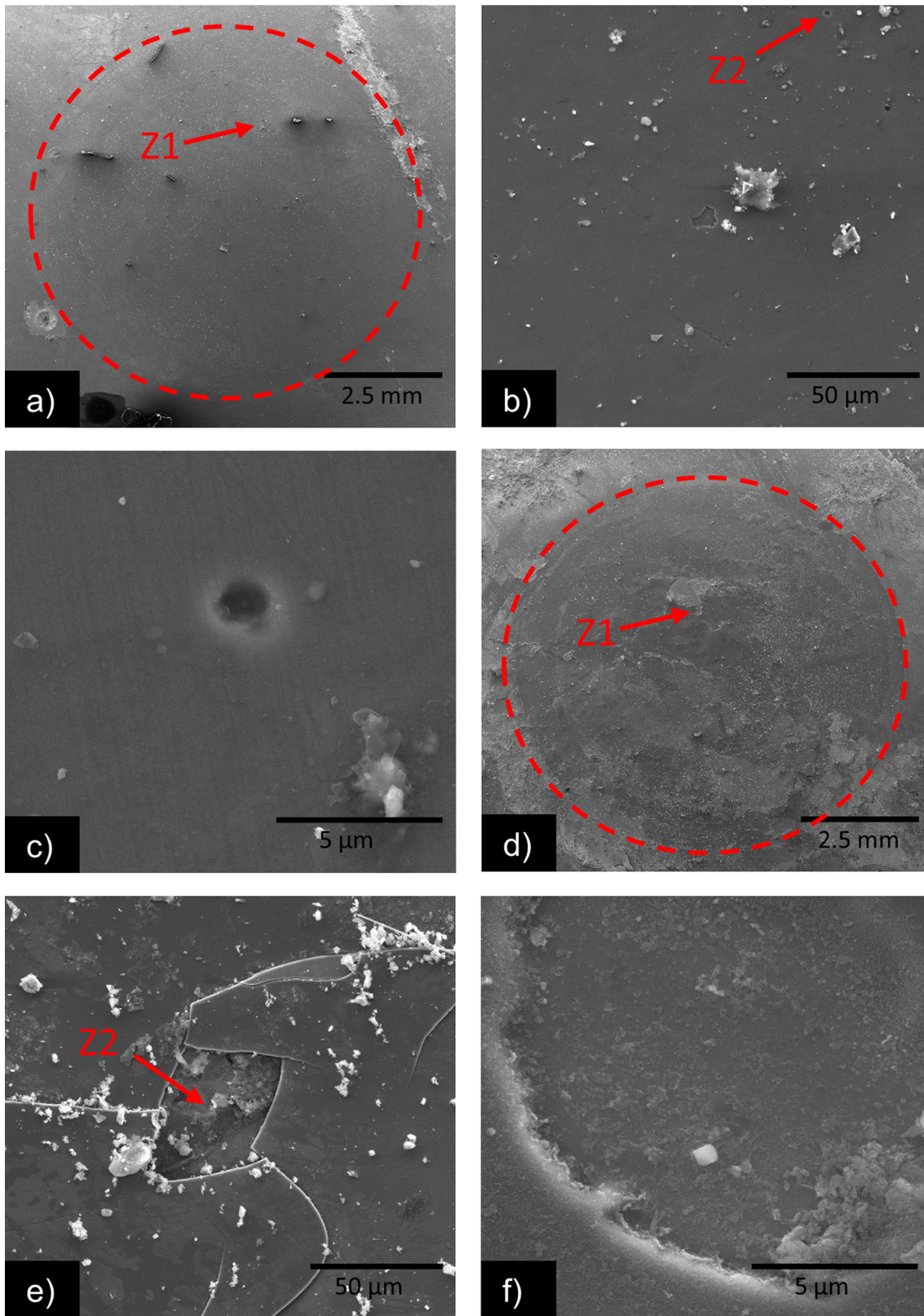


Figure 7 (a) Corrosion track for sample *S4*, (b) Ampliation of Zone 1 and (c) Ampliation of Zone 2. (d) Corrosion tracks for sample *S5*, (e) Ampliation of Zone 1 and (f) Ampliation of Zone 2

due to the presence of a $a\text{-CN}_x$ phase. The multilayers with different architecture proposed, with thickness of 1.5 and 1.2 μm in this investigation improved the corrosion properties

of the AISI-A11 steel substrate, being a potential protective surface for corrosion environments such as moving parts during machining and cutting tools.

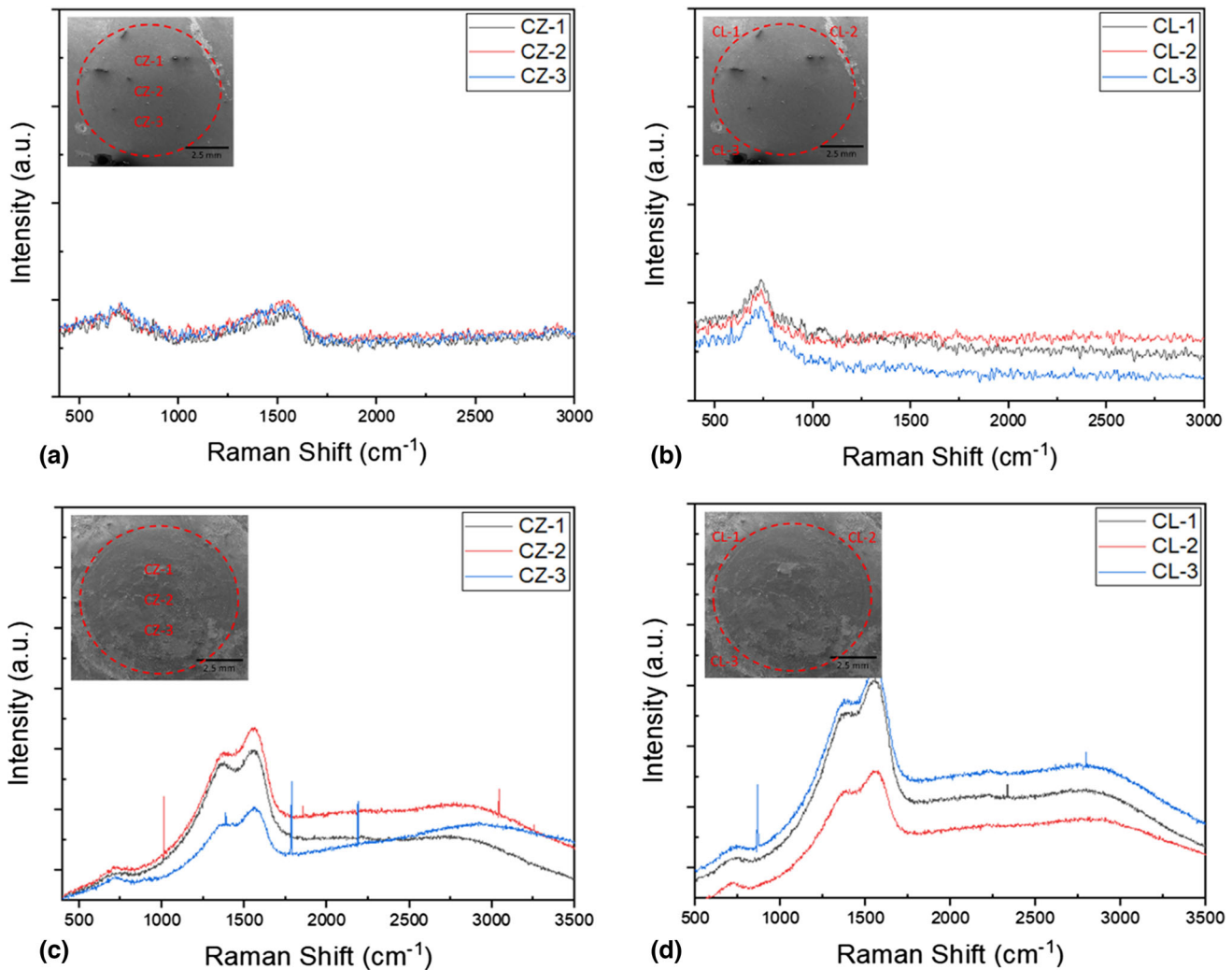


Figure 8 Raman analysis after corrosion test in sample *S4*. (a) Corrosion Zone, (b) Corrosion Line. Raman analysis after corrosion analysis after corrosion test in sample *S5*. (c) Corrosion Zone and (d) Corrosion Line

Acknowledgments

Cecilio J. Martínez-Gonzalez wants to thank Mexican National Council of Science and Technology (CONACYT-Mexico) for providing the funding for this research project. Also, Cecilio J. Martínez-Gonzalez wants to thank to the Maestría en Ciencia e Ingeniería de los Materiales, Quantum-Ciudad del Conocimiento de la Universidad Autónoma de Zacatecas for assisting with the XRD and XRF laboratory facilities.

Authors' Contribution

CJM-G contributed to methodology, investigation, writing—original draft. M. Flores-Jimenez: Formal analysis, Project administration. J.P-A: Validation, data curation. OJ contributed to resources, supervision, writing—review and editing. MF contributed to resources, supervision.

Conflict of interest

The authors declare that they have no known competing financial interests or personal relationships that could have

appeared to influence the work reported in this paper.

References

1. B.C. Schramm, H. Scheerer, H. Hoche, E. Broszeit, E. Abele, and C. Berger, Tribological Properties and Dry Machining Characteristics of PVD-Coated Carbide Inserts, *Surf. Coatings Technol.*, 2004, **188–189**, p 623–629. <https://doi.org/10.1016/j.surfcoat.2004.07.067>
2. U. Schleinkofer, C. Czettl, and C. Michotte, Coating Applications for Cutting Tools, Elsevier Ltd, 2014. <https://doi.org/10.1016/B978-0-08-096527-7.00016-7>
3. A.A. Chavan and P.V. Deshmukh, Prediction of Tool Life of Different Coated Cutting Tools During Machining of Inconel 718, *Int. Res. J. Eng. Technol.*, 2017, **4**(941), p 949
4. K. Reichelt and X. Jiang, The Preparation of Thin Films by Physical Vapour Deposition Methods, *Thin Solid Films*, 1990, **191**, p 91–126. [https://doi.org/10.1016/0040-6090\(90\)90277-K](https://doi.org/10.1016/0040-6090(90)90277-K)
5. B. Matthes, E. Broszeit, J. Aromaa, H. Ronkainen, S.P. Hannula, A. Leyland, and A. Matthews, Corrosion Performance of Some Titanium-Based Hard Coatings, *Surf. Coatings Technol.*, 1991, **49**, p 489–495. [https://doi.org/10.1016/0257-8972\(91\)90105-6](https://doi.org/10.1016/0257-8972(91)90105-6)
6. F. Jiang, T.F. Zhang, B.H. Wu, Y. Yu, Y.P. Wu, S.F. Zhu, F.J. Jing, N. Huang, and Y.X. Leng, Structure, Mechanical and Corrosion Properties of TiN Films Deposited on Stainless Steel Substrates with Different Inclination Angles by DCMS and HPPMS, *Surf. Coatings Technol.*, 2016, **292**, p 54–62. <https://doi.org/10.1016/j.surfcoat.2016.03.007>

7. G. Berg, C. Friedrich, E. Broszeit, and C. Berger, Development of Chromium Nitride Coatings Substituting Titanium Nitride, *Surf. Coatings Technol.*, 1996, **86–87**, p 184–191. [https://doi.org/10.1016/S0257-8972\(96\)03042-3](https://doi.org/10.1016/S0257-8972(96)03042-3)
8. G. Bertrand, H. Mahdjoub, and C. Meunier, A Study of the Corrosion Behaviour and Protective Quality of Sputtered Chromium Nitride coatings, *Surf. Coatings Technol.*, 2000, **126**, p 199–209. [https://doi.org/10.1016/S0257-8972\(00\)00527-2](https://doi.org/10.1016/S0257-8972(00)00527-2)
9. D. Liu, H. Ma, H. Li, and Y. Liang, Structure, Phase Transformation and Corrosion Resistance of CrAlN/CN_x Composite Multilayer Films in NaCl Aqueous Solution, *Ceram. Int.*, 2019, **45**, p 24446–24452. <https://doi.org/10.1016/j.ceramint.2019.08.169>
10. J. Pérez-Alvarez, M. Flores-Jiménez, C.D. Rivera-Tello, R. Suárez-Martínez, O. Jiménez, L. Flores-Cova, and M. Flores, Effect of a-CN_x top Layer on the Electrochemical Properties of Ta₂N/Ta Multilayers Obtained by HIPIMS, *Mater. Lett.*, 2020, **278**, p 1–5. <https://doi.org/10.1016/j.matlet.2020.128454>
11. F. Zhou, K. Fu, B. Liao, J. Yu, C. Yang, and X. Zhang, Effect of Carbon Content on Nanostructural, Mechanical and Electrochemical Characteristics of Self-organized nc-ZrCN/a-CN_x Nanocomposite Films, *Appl. Surf. Sci.*, 2015, **327**, p 350–357. <https://doi.org/10.1016/j.apsusc.2014.11.181>
12. P. Panjan, Industrial Applications of CrN (PVD) Coatings, Deposited at High and Low Temperatures, *Surf. Coatings Technol.*, 1997, **97**, p 182–191
13. J.F. Tang, C.Y. Lin, F.C. Yang, and C.L. Chang, Influence of Nitrogen Content and Bias Voltage on Residual Stress and the Tribological and Mechanical Properties of CrAlN Films, *Coatings*, 2020 <https://doi.org/10.3390/COATINGS10060546>
14. J.Z. Kong, T.J. Hou, Q.Z. Wang, L. Yin, F. Zhou, Z.F. Zhou, and L.K.Y. Li, Influence of Titanium or Aluminum Doping on the Electrochemical Properties of CrN Coatings in Artificial Seawater, *Surf. Coatings Technol.*, 2016, **307**, p 118–124. <https://doi.org/10.1016/j.surfcoat.2016.08.036>
15. O.M.S. Quintero, W.A. Chaparro, L. Ipaz, J.E.S. Barco, F.E. Beltrán, and G. Zambrano, Influence of the Microstructure on the Electrochemical Properties of Al-Cr-N Coatings Deposited by Co-Sputtering Method from a Cr-Al Binary Target, *Mater. Res.*, 2013, **16**, p 204–214. <https://doi.org/10.1590/S1516-14392012005000171>
16. X. Zhao Ding, A.L.K. Tan, X.T. Zeng, C. Wang, T. Yue, and C.Q. Sun, Corrosion Resistance of CrAlN and TiAlN Coatings Deposited by Lateral Rotating Cathode Arc, *Thin Solid Films.*, 2008, **516**, p 5716–5720. <https://doi.org/10.1016/j.tsf.2007.07.069>
17. Y.C. Chim, X.Z. Ding, X.T. Zeng, and S. Zhang, Oxidation Resistance of TiN, CrN, TiAlN and CrAlN Coatings Deposited by Lateral Rotating Cathode Arc, *Thin Solid Films*, 2009, **517**, p 4845–4849. <https://doi.org/10.1016/j.tsf.2009.03.038>
18. S. Khamseh, M. Nose, T. Kawabata, K. Matsuda, and S. Ikeno, Oxidation Resistance of CrAlN Films with Different Microstructures Prepared by Pulsed DC Balanced Magnetron Sputtering System, *Mater. Trans.*, 2010, **51**, p 271–276. <https://doi.org/10.2320/matertrans.MC200912>
19. C. Nouveau, B. Tlili, H. Aknouche, Y. Benlatreche, and B. Patel, Comparison of CrAlN Layers Obtained with One (CrAl) or Two Targets (Cr and Al) by Magnetron Sputtering, *Thin Solid Films*, 2012, **520**, p 2932–2937. <https://doi.org/10.1016/j.tsf.2011.11.049>
20. S.H. Tsai and J.G. Duh, Microstructure and Corrosion Properties of Multilayered CrAlN/SiN_x Coatings, *J. Electrochem. Soc.*, 2010, **157**, p K89. <https://doi.org/10.1149/1.3321761>
21. N.E. Beliaidouh, K. Bouzid, C. Nouveau, B. Tlili, and M.J. Walock, Tribological and Electrochemical Performances of Cr/CrN and Cr/CrN/CrAlN Multilayer Coatings Deposited by RF Magnetron Sputtering, *Tribol. Int.*, 2015, **82**, p 443–452. <https://doi.org/10.1016/J.TRIBOINT.2014.03.018>
22. L. Ipaz, W. Aperador, J. Caicedo, J. Esteve, and G. Zambrano, A Practical Application of X-Ray Spectroscopy in Ti-Al-N and Cr-Al-N Thin Films, *X-Ray Spectrosc.*, 2012 <https://doi.org/10.5772/29640>
23. P.E. Hovsepian, C. Reinhard, and A.P. Ehiasarian, CrAlYN/CrN Superlattice Coatings Deposited by the Combined High Power Impulse Magnetron Sputtering/Unbalanced Magnetron Sputtering Technique, *Surf. Coatings Technol.*, 2006, **201**, p 4105–4110. <https://doi.org/10.1016/j.surfcoat.2006.08.027>
24. J. Paulitsch, P.H. Mayrhofer, W.D. Münz, and M. Schenkel, Structure and Mechanical Properties of CrN/TiN Multilayer Coatings Prepared by a Combined HIPIMS/UBMS Deposition Technique, *Thin Solid Films*, 2008, **517**, p 1239–1244. <https://doi.org/10.1016/j.tsf.2008.06.080>
25. M. Samuelsson, D. Lundin, J. Jensen, M.A. Raadu, J.T. Gudmundsson, and U. Helmersson, On the Film Density Using High Power Impulse Magnetron Sputtering, *Surf. Coatings Technol.*, 2010, **205**, p 591–596. <https://doi.org/10.1016/J.SURFCOAT.2010.07.041>
26. J. Paulitsch, M. Schenkel, T. Zuffraß, P.H. Mayrhofer, and W.D. Münz, Structure and Properties of High Power Impulse Magnetron Sputtering and DC Magnetron Sputtering CrN and TiN Films Deposited in an Industrial Scale Unit, *Thin Solid Films*, 2010, **518**, p 5558–5564. <https://doi.org/10.1016/j.tsf.2010.05.062>
27. M.A. and R.C. Böhlmark, Grzegorz Greczynski, and Johan, Y.T. Pei, C.Q. Chen and Jeff Th. M. De Hosson, High Power Impulse Magnetron Sputtering for Industrial Applications: Deposition of Chromium Films on Inclined Surfaces, 2008. www.vatvalve.com. Accessed May 6, 2021
28. K. Bobzin, T. Brögelmann, N.C. Kruppe, M. Engels, A. Von Keudell, A. Hecimovic, A. Ludwig, D. Grochla, and L. Banko, Fundamental Study of an Industrial Reactive HPPMS (Cr, Al)N Process, *J. Appl. Phys.*, 2017 <https://doi.org/10.1063/1.4990997>
29. N.A. Baseri, M. Mohammadi, M. Ghatee, M. Abassi-Firouzjah, and H. Elmkhah, The Effect Of Duty Cycle on the Mechanical and Electrochemical Corrosion Properties of Multilayer CrN/CrAlN Coatings Produced by Cathodic Arc Evaporation, *Surf. Eng.*, 2021, **37**, p 253–262. <https://doi.org/10.1080/02670844.2020.1775331>
30. Z. Zhao, Q. Miao, W. Liang, J. Xia, H. Lin, Y. Qi, and S. Zuo, Effect of CrAl Interlayer on Adhesion Strength of CrAlN Coating, *Surf. Eng.*, 2020, **36**, p 438–446. <https://doi.org/10.1080/02670844.2019.1672956>
31. K.D. Bakoglidis, S. Schmidt, G. Greczynski, and L. Hultman, Improved Adhesion of Carbon Nitride Coatings on Steel Substrates Using Metal HiPIMS Pretreatments, *Surf. Coatings Technol.*, 2016, **302**, p 454–462. <https://doi.org/10.1016/j.surfcoat.2016.06.048>
32. X. Hua Zheng, F. Er Yang, L. Chen, Z. Ling Chen, R. Guo Song, and X. Hua Zhang, Microstructure and Mechanical Properties of a-CN_x Films Prepared by Bias Voltage Assisted PLD with Carbon Nitride Target, *Surf. Coatings Technol.*, 2014, **258**, p 716–721. <https://doi.org/10.1016/j.surfcoat.2014.08.009>
33. K.D. Bakoglidis, S. Schmidt, M. Garbrecht, I.G. Ivanov, J. Jensen, G. Greczynski, and L. Hultman, Low-Temperature Growth of Low Friction Wear-Resistant Amorphous Carbon Nitride Thin Films by Mid-Frequency, High Power Impulse, and Direct Current Magnetron Sputtering, *J. Vac. Sci. Technol. A Vacuum Surfaces Film.*, 2015, **33**, p 05112. <https://doi.org/10.1116/1.4923275>
34. A.C. Ferrari, S.E. Rodil, and J. Robertson, Interpretation of Infrared and Raman Spectra of Amorphous Carbon Nitrides, *Phys. Rev.*, 2003 <https://doi.org/10.1103/PhysRevB.67.155306>
35. A. Vyas, Z.F. Zhou, and Y.G. Shen, Effect of Aluminum Contents on Sputter Deposited CrAlN Thin Films, *IOP Conf. Ser. Mater. Sci. Eng.*, 2018 <https://doi.org/10.1088/1757-899X/307/1/012079>
36. J.A. Taylor, An XPS Study of the Oxidation of AlAs Thin Films Grown by MBE, *J. Vac. Sci. Technol.*, 1998, **20**, p 751. <https://doi.org/10.1116/1.571450>
37. J.L. Endrino, G.S. Fox-Rabinovich, A. Reiter, S.V. Veldhuis, R. Escobar Galindo, J.M. Albella, and J.F. Marco, Oxidation Tuning in AlCrN Coatings, *Surf. Coatings Technol.*, 2007, **201**, p 4505–4511. <https://doi.org/10.1016/J.SURFCOAT.2006.09.089>
38. O. Nishimura, K. Yabe, and M. Iwaki, X-Ray Photoelectron Spectroscopy Studies of High-Dose Nitrogen Ion Implanted-Chromium: A Possibility of a Standard Material for Chemical State Analysis, *J. Electron Spectros. Relat. Phenomena.*, 1989, **49**, p 335–342. [https://doi.org/10.1016/0368-2048\(89\)85021-2](https://doi.org/10.1016/0368-2048(89)85021-2)
39. H.C. Barshilia, N. Selvakumar, B. Deepthi, and K.S. Rajam, A Comparative Study of Reactive Direct Current Magnetron Sputtered CrAlN and CrN Coatings, *Surf. Coatings Technol.*, 2006, **201**, p 2193–2201. <https://doi.org/10.1016/J.SURFCOAT.2006.03.037>
40. X.C. Wang, Z.Q. Li, P. Wu, E.Y. Jiang, and H.L. Bai, Structural and Mechanical Properties of Facing-Target Sputtered Amorphous CN_x Films, *Diamond Relat. Mater.*, 2006, **15**(1732), p 1737. <https://doi.org/10.1016/j.diamond.2006.03.002>
41. F.E. Yang, S.Y. Yang, X.X. Chang, W.F. Yang, R.G. Song, and X.H. Zheng, Microstructure and Properties of DLC/CN_x Films with Different CN_x Sublayer Thicknesses, *Surf. Coatings Technol.*, 2019, **374**, p 418–423. <https://doi.org/10.1016/j.surfcoat.2019.06.011>

42. P. Jurčí, J. Bohovičová, M. Hudáková, and P. Bílek, Characterization and Wear Performance of CrAgN Thin Films Deposited on Cr-V Ledeburitic Tool Steel, *Mater. Tehnol.*, 2014, **48**, p 159–170
43. L. Wang, G. Zhang, R.J.K. Wood, S.C. Wang, and Q. Xue, Fabrication of CrAlN Nanocomposite Films with High Hardness and Excellent Anti-Wear Performance for Gear Application, *Surf. Coatings Technol.*, 2010, **204**, p 3517–3524. <https://doi.org/10.1016/j.surfcoat.2010.04.014>
44. M. Zhou, Y. Makino, M. Nose, and K. Nogi, Phase Transition and Properties of Ti-Al-N Thin Films prepared by r.f.-Plasma Assisted Magnetron Sputtering, *Thin Solid Films*, 1999, **339**, p 203–208. [https://doi.org/10.1016/S0040-6090\(98\)01364-9](https://doi.org/10.1016/S0040-6090(98)01364-9)
45. N. Laegreid and G.K. Wehner, Sputtering Yields of Metals for Ar⁺ and Ne⁺ Ions with Energies from 50 to 600 eV, *J. Appl. Phys.*, 1961, **32**, p 365–369. <https://doi.org/10.1063/1.1736012>
46. D. Wang, S. Lin, L. Liu, H. Yang, J. Shi, B. Jiang, K. Zhou, and X. Zhang, Micro-Nano Multilayer Structure Design and Solid Particle Erosion Resistance Performance of CrAlN_x/CrAlN Coating, *Vacuum*, 2020, **172**, p 109064. <https://doi.org/10.1016/j.vacuum.2019.109064>
47. D. Wang, S.S. Lin, Q. Shi, Y.N. Xue, H.Z. Yang, D.C. Zhang, Z.Z. Xu, C.Q. Guo, M.J. Dai, B.L. Jiang, and K.S. Zhou, Microstructure Effects on Fracture Failure Mechanism of CrAl/CrAlN Coating, *Ceram. Int.*, 2021, **47**(3), p 3657–3664. <https://doi.org/10.1016/j.ceramint.2020.09.217>
48. L.L.G. da Silva, M. Ueda, and R.Z. Nakazato, Enhanced Corrosion Resistance of AISI H13 Steel Treated by Nitrogen Plasma Immersion Ion Implantation, *Surf. Coatings Technol.*, 2007, **201**, p 8291–8294. <https://doi.org/10.1016/J.SURFCOAT.2006.03.063>
49. S.H. Tsai, J.G. Duh, C.H. Lin, and J.G. Duh, Electrochemical Impedance Spectroscopy (EIS) Study on Corrosion Performance of CrAlSiN Coated Steels in 3.5 wt.% NaCl Solution, *J. Electrochem. Soc.*, 2010, **157**, p K89. <https://doi.org/10.1149/1.3321761>
50. C.H. Lin and J.G. Duh, Electrochemical Impedance Spectroscopy (EIS) Study on Corrosion Performance of CrAlSiN Coated Steels in 3.5 wt.% NaCl Solution, *Surf. Coatings Technol.*, 2009, **204**, p 784–787. <https://doi.org/10.1016/j.surfcoat.2009.09.059>
51. K.T.K. Chiang and R. Wei, Growth Morphology and Corrosion Resistance of Magnetron Sputtered Cr Films, *Surf. Coatings Technol.*, 2011, **206**, p 1660–1665. <https://doi.org/10.1016/j.surfcoat.2011.09.020>
52. W. Tato and D. Landolt, Electrochemical Determination of the Porosity of Single and Duplex PVD Coatings of Titanium and Titanium Nitride on Brass, *J. Electrochem. Soc.*, 1998, **145**, p 4173–4181. <https://doi.org/10.1149/1.1838932>
53. Z. Wu, Z. Cheng, H. Zhang, Z. Xu, Y. Wang, and F. Zhou, Electrochemical and Tribological Properties of CrAlN, TiAlN, and CrTiN Coatings in Water-Based Cutting Fluid, *J. Mater. Eng. Perform.*, 2020, **29**, p 2153–2163. <https://doi.org/10.1007/s11665-020-04772-3>
54. M. Kaliwoda, D. Giordano, M.E. Kruger, I. Uysal, M.R. Akmaz, V. Hoffmann, R. Hochleitner, and W.W. Schmahl, Raman Spectroscopy as a Tool for the Quantitative Estimation of Chromium Aluminum Oxide Content in Chromite, *Spectroscopy*, 2021, **36**, p 17
55. Chromite-Magnesiochromite Series: Mineral information, data and localities., (n.d.). <https://www.mindat.org/min-8675.html>. Accessed December 4, 2022
56. M. Mehrooz, G.C. Kirkwood, S. Scheinman, G.T. Bayer, Corrosion Sensors For Detecting Graphitization Of Cast Iron In Water Mains, (2007). /NACECORR/proceedings-abstract/CORR07/All-CORR07/127563 (accessed December 4, 2022)
57. J.L. Gallego, L.M. Franco, H. Riascos, C. Vargas-Hernández, and R. Ospina, Caracterización Raman y EDX de películas delgadas de CrN crecidas por ablación láser, *Rev. Latinoam. Metal. y Mater.*, 2009, **29**, p 109–114
58. A. Ferrari and J. Robertson, Interpretation of Raman Spectra of Disordered and Amorphous Carbon, *Phys Rev. B - Condens. Matter Mater. Phys.*, 2000, **61**, p 14095–14107. <https://doi.org/10.1103/PhysRevB.61.14095>
59. M. Rebelo de Figueiredo, C. Bergmann, C. Ganser, C. Teichert, C. Kukla, and C. Mitterer, Adhesion Tendency of Polymers to Hard Coatings, *Int. Polym. Process.*, 2013, **28**, p 415–420. <https://doi.org/10.3139/217.2767>

Publisher's Note Springer Nature remains neutral with regard to jurisdictional claims in published maps and institutional affiliations.

Springer Nature or its licensor (e.g. a society or other partner) holds exclusive rights to this article under a publishing agreement with the author(s) or other rightsholder(s); author self-archiving of the accepted manuscript version of this article is solely governed by the terms of such publishing agreement and applicable law.